Sustainable Cities and Society 118 (2025) 106011

Contents lists available at ScienceDirect

Sustainable Cities and Society

journal homepage: www.elsevier.com/locate/scs

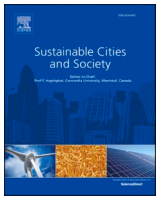

Shade watch: Mapping citywide shade dynamics through ray tracing and LiDAR data in Hong Kong's complex 3-D built environment

Shengbiao Wu [a], Bin Chen [a,b,c,*], Yimeng Song [d], Jiafu An [c,e], Chen Lin [b,c,f], Peng Gong [b,c,g]

[a] Future Urbanity & Sustainable Environment (FUSE) Lab, Division of Landscape Architecture, Department of Architecture, Faculty of Architecture, The University of Hong Kong, Hong Kong SAR, China
[b] Urban Systems Institute, The University of Hong Kong, Hong Kong SAR, China
[c] Institute for Climate and Carbon Neutrality, The University of Hong Kong, Hong Kong SAR, China
[d] School of the Environment, Yale University, New Haven, CT, United States
[e] Department of Real Estate and Construction, Faculty of Architecture, The University of Hong Kong, Hong Kong SAR, China
[f] Faculty of Business and Economics, The University of Hong Kong, Hong Kong SAR, China
[g] Department of Geography and Department of Earth Sciences, The University of Hong Kong, Hong Kong SAR, China

ARTICLE INFO

Keywords:
Heat stress
Sunlight hour
Digital surface model
Urban morphology
Landscape configuration

ABSTRACT

The importance of urban shade in city planning has been underscored by its various associations with thermal comfort, living environment quality, human health and well-being. However, existing methods for urban shade mapping are often limited to street-level scopes or singular sampling observational times, leaving citywide shade mapping, its spatiotemporal patterns, and controlling factors largely unexplored. To fill these knowledge gaps, this study proposed a novel protocol that enables seamless mapping of spatiotemporal urban shade patterns over the entire city by fusing look-up-table (LUT)-based ray-tracing approach with Google Earth Engine cloud computing technology, as well as high-resolution digital surface model (DSM) derived from LiDAR data. This protocol was applied to Hong Kong, a city characterized by complex 3-D built environments, and then delved into the spatiotemporal patterns of urban shade and the associated controlling factors. Validation results indicate that the proposed method can accurately quantify urban shade compared to ground-based photo references and high-resolution satellite imagery. The analysis uncovers that: (1) Shade exhibits spatial heterogeneity across different 3-D built environments while maintaining a consistent "U-shape" diurnal shade fraction during the day; (2) Solar geometry, regardless of solar zenith and azimuth angle, is negatively associated with aggregated metrics of shade landscape and positively associated with fragmented metrics. Moreover, solar zenith angles exert stronger controls over the citywide shade landscape patterns; and (3) Persistent shade significantly reduces the sunlight hours (i.e., the accumulated sunshine hours per day) across administrative districts, local climate zones (LCZs), and seasons. Due to shade effects originating from 3-D urban structures, Hong Kong typically experiences an average of 4–8 sunlight hours per day within a one-year cycle, which is substantially lower than the 11–14 h of natural daylength. This study offers a practical protocol for large-scale urban shade mapping, enhancing our understanding of urban shade, its spatiotemporal dynamics, and benefits in a broader spatiotemporal context. The associated datasets and findings from this study can inform urban planners and policymakers in developing effective strategies to create healthier and sustainable urban environments in Hong Kong.

1. Introduction

Shade is a ubiquitous natural phenomenon that objects on Earth, when illuminated by the Sun or other artificial light sources (e.g., incandescent lamps and light-emitting diodes), can project light-blocking areas to their neighbors (cast shadow) and experience self-shadowing due to their 3-D morphology (Kaňuk et al. 2015). The unique roles of shade in complex 3-D urban environments have aroused increasing attention (Gomez-Muñoz et al. 2010; Horváthová et al. 2021) due to its various impacts on socio-economic-environmental dimensions of cities,

* Corresponding author.
E-mail address: binley.chen@hku.hk (B. Chen).

https://doi.org/10.1016/j.scs.2024.106011
Received 14 January 2024; Received in revised form 17 October 2024; Accepted 22 November 2024
Available online 23 November 2024
2210-6707/© 2024 Elsevier Ltd. All rights are reserved, including those for text and data mining, AI training, and similar technologies.

such as modifying urban heat environments (Donovan and Butry, 2009; Speak et al. 2020), influencing human health and well-being (Jay et al. 2021; Schneider et al. 2020), and changing residents' perceptions and preferences of living conditions (Gwedla and Shackleton, 2019; Lo and Jim, 2015).

Urban shade is widely recognized for its ability to reduce air temperature and promote outdoor human thermal comfort by obstructing direct sunlight and inhibiting heat absorption and release by surfaces (Gómez-Muñoz et al. 2010; Speak et al. 2020). Vegetation, such as trees, can contribute to shade and evapotranspiration, helping alleviate urban heat stress (Middel et al. 2021; Wong et al. 2021; Ziter et al. 2019). Recent studies suggest that shading may have greater potential in cooling surfaces than evapotranspiration (Tan et al. 2018). Moreover, the 3-D structure of built-up areas can cast shadows on the ground, blocking direct sunlight and potentially reducing the urban heat island effect, even leading to an overall cooling effect (Alhazmi et al. 2022; Park et al. 2021). Both natural and artificial shading can significantly lower surface temperatures by 5–7 °C, equivalent to a 7–15 °C reduction in physiologically equivalent temperature (Armson et al. 2012; Elgheznawy and Eltarabily, 2021; Horváthová et al. 2021). The magnitude of these temperature reductions is influenced by factors like vegetation characteristics (e.g., types, age, species, and 3-D structure; De Abreu-Harbich et al. 2015; Gómez-Muñoz et al. 2010), built-up properties (e.g., size, shape, location, density, and spatial arrangement; Colter et al. 2019; Taleghani et al. 2021), and weather conditions (Cheung and Jim, 2019; Wang et al. 2019).

Urban shade is closely linked to human health and well-being (Gage et al. 2018; Schneider et al. 2020). The presence of shade can protect against excessive exposure to solar ultraviolet radiation and reduce the risk of sunburn and skin cancer (Gilchrist et al. 2020; Sivarajah et al. 2020). Shade is particularly important in school playgrounds, where children are more vulnerable to heat stress due to their higher metabolic activities and underdeveloped body regulatory mechanisms compared to adults (Cherian and Subasinghe, 2022; Olsen et al. 2019; Xu et al. 2012). As a result, shade provision has been specified as a key metric in policies and practices for school playground safety (Holman et al. 2018). However, excessive shade (i.e., insufficient sunshine time) can also have negative effects on public health. Limited exposure to sunlight has been highly associated with a high prevalence of vitamin D deficiency (Bouillon, 2020; Mogire et al. 2020). Additionally, urban shade significantly influences residents' perception of their surroundings and can affect their preferences for physical activities (Gwedla and Shackleton, 2019; Mehta, 2008). For example, recent biometeorological research has shown that people generally choose to walk along shaded streets during hot summer days (Lee et al. 2020); during winter or spring, many people prefer sunnier spots (Mehta, 2008). Therefore, a better understanding of the spatiotemporal urban shade patterns is highly required to inform and further advance these studies.

Existing shade mapping approaches can be broadly classified into two types: backward extraction (Luo et al. 2020; Li and Ratti, 2018; Li et al. 2018; Zhang et al. 2020) and forward simulation (Lindberg and Grimmond, 2010; Park et al. 2021; Ratti and Richens, 2004; Yu et al. 2020) methods. The backward extraction method relies on available observations from Google Street View (GSV) panorama photographs or satellite imagery and uses photographic or machine learning algorithms to detect urban shade. While this method provides accurate shade phenomena, it only offers discrete spatial coverage at individual sites or frequency at specific observational times (Biljecki and Ito; Gage et al. 2018). For instance, the GSV panorama captures only a few fractions of the 3-D urban environment within its viewing extent, resulting in the extracted shade being discontinuous and disconnected and limiting shade-based analysis and applications. On the other hand, the forward simulation method calculates shade maps from 3-D digital surface models (DSM) or building models using hillshade analysis (a topographic shade analytical tool; Yu et al. 2020) or shade casting (Lindberg and Grimmond, 2010) algorithms. Theoretically, this method can provide spatially seamless urban shade maps for any given time, and it is widely used for local-level shade and its cooling benefit quantification, supported by Geographic Information System (GIS) platforms (Buo et al. 2023; Troy et al. 2024). However, these GIS tools remain challenging for mapping citywide shade over space and time due to the lack of high-resolution LiDAR data and large computational time required to account for varying solar locations (e.g., diurnal and seasonal dynamics). For example, generating an urban shade map for a 36 km^2 area with a 2-m resolution raster 3-D city model, for one hour with a 30-minute interval, could take up to 84 h (Park et al. 2021). Due to the challenges in the algorithm development of large-scale urban shade mapping and data products, our current understanding of the spatiotemporal heterogeneity of urban shade, its blocking effects on sunlight time, and the associated underlying controlling mechanism at the city scale is largely limited.

To address the challenges mentioned above, this study proposed a novel protocol that allows for mapping citywide urban shades by combing look-up-table (LUT)-based ray-tracing approach with Google Earth Engine cloud computing technology, as well as high-resolution DSM data. Specifically, following the annual trajectory of solar position, the proposed approach divides solar azimuth angle into equal bins (e.g., 57 bins with a 5° interval for summertime in Hong Kong), and maps the pixel-level, angular-bin-based LUTs of horizon angle (i.e., the maximum zenith angle of target can be sunlit considering its neighboring blocking effects). By comparing these raster LUTs of horizontal angles with actual solar geometry (i.e., solar zenith angle), shade conditions for any given time can be mapped. To enhance computational efficiency, the LUTs of horizontal angles were deployed on the GEE cloud computing platform for citywide shade mapping. Hong Kong was selected as an experimental city for testing this proof-of-concept due to its high-rise, high-density urban environment and the availability of a 0.5-m resolution airborne LiDAR dataset. Specifically, this study aims to address three key research questions: (1) How can we efficiently map citywide shade? (2) What are the spatiotemporal patterns of urban shade across the entire city? (3) What factors influence the landscape patterns of urban shade?

2. Materials and methods

2.1. Study design

The methodology in this study includes three major tasks (Fig. 1): (1) the development of citywide shade mapping approach; (2) spatiotemporal analysis of urban shade; and (3) association analysis between solar geometry and shade landscapes.

2.2. Study area

Hong Kong is an administrative region located on the eastern side of the mouth of the Chinese Pearl River estuary, situated 60 km to the east of Macau. It is bordered by the South China Sea and shares its boundary with Shenzhen. With a total land area of approximately 1104 km^2, Hong Kong is divided into 18 administrative districts. This city experiences a humid subtropical climate characterized by a long hot-humid summer from June to August, and a short mild winter from December to February. The average annual maximum air temperate and precipitation of Hong Kong are 33 °C and 2400 mm (Shi et al. 2019), respectively. Hong Kong is a highly developed and densely-populated city with about 7.5 million residents of various nationalities (~7000 people/km^2 in metro area on average, Hua et al. 2021). Hong Kong is selected as study area due to its complex 3-D built environment and the availability of high-resolution LiDAR datasets.

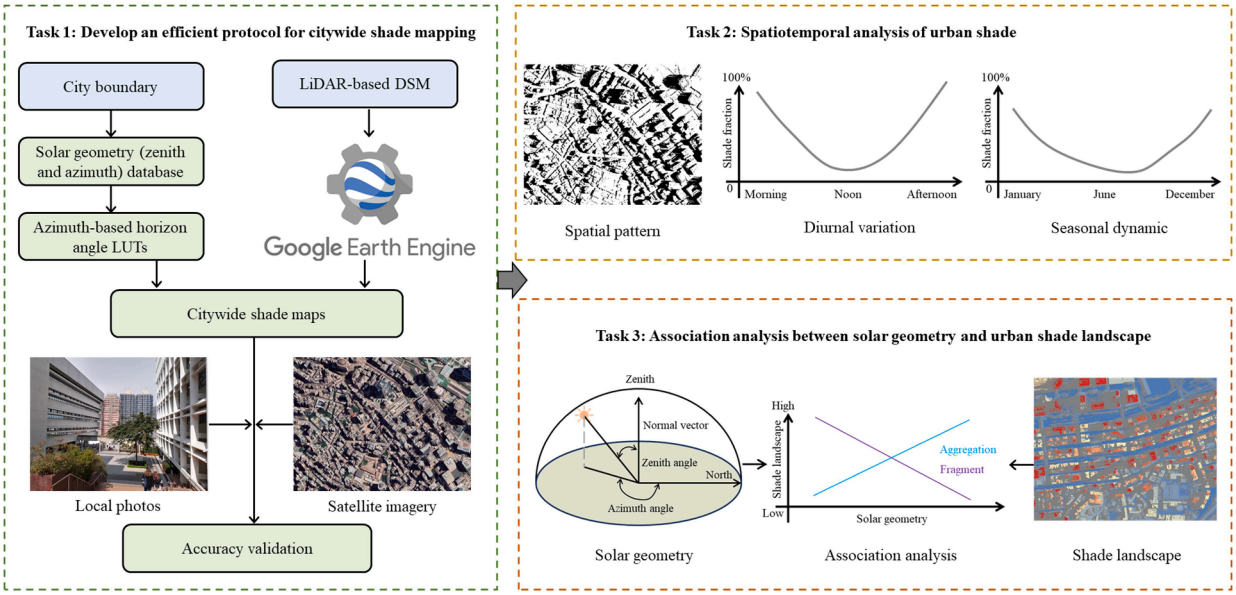

Fig. 1. Flowchart of the methodology used in this study, including three sub-tasks: (1) the development of citywide shade mapping approach; (2) spatiotemporal analysis of urban shade; and (3) association analysis between solar geometry and shade landscapes.

2.3. Datasets

2.3.1. 3-D LiDAR data

This study used the 0.5-m resolution LiDAR data from the Survey and Mapping Office (SMO) of the Lands Department (LandsD) and the Survey Division of Civil Engineering and Development Department (CEDD) to create urban shade maps for Hong Kong. CEDD provides two collections of airborne LiDAR cloud point datasets, which were measured between December 2010 to January 2011 (LiDAR Data-2010) and December 2019 to February 2020 (LiDAR Data-2020), respectively. These two LiDAR datasets have a maximum point spacing of 0.5 m, with a horizontal and vertical accuracy of 0.3 m and 0.1 m, respectively (Chan et al. 2021). The DSM extracted from the LiDAR Data-2020 dataset was selected, which is available in a GeoTiff raster format and can be accessed through the Hong Kong GeoData Store at https://geodata.gov.hk/gs/. A total of 3315 DSM grid tiles, covering the entire Hong Kong region, were downloaded and utilized in this study (Fig. 2).

2.3.2. Ground-based photo references

To validate the accuracy of the DSM-derived shade mappings, two ground-based pictures on clear-sky days were used as reference (Table 1). The first photo was captured at 14:37:45 on February 6, 2023, in front of the Bonham mansion building (22°17′04″N, 114°08′27″E) along Bonham Road. The second photo was taken at 13:19:14 on February 11, 2023, in Sun Yat Sen Place (22°17′00″N, 114°08′17″E) that located in the University of Hong Kong (HKU) campus.

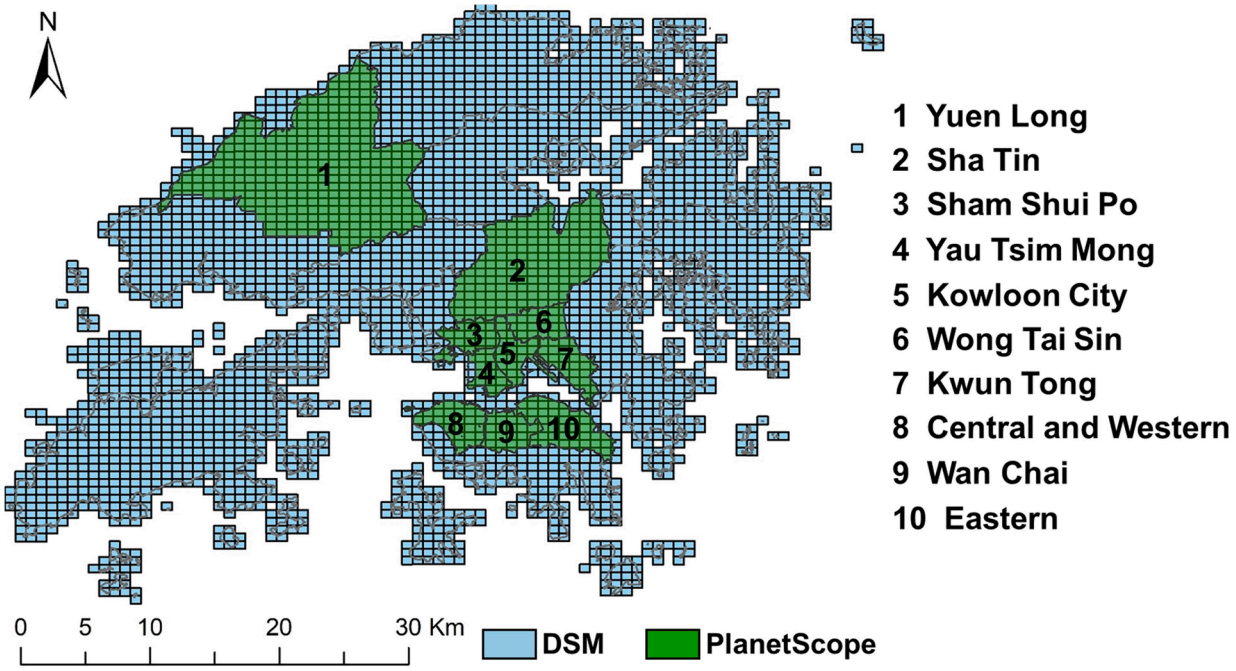

Fig. 2. Hong Kong's 0.5-m resolution DSM data (blue rectangles) used for urban shade mapping and 3-m resolution PlanetScope imagery over ten administrative districts (green polygons) used for shade accuracy validation.

Table 1
Datasets used for the accuracy validation of the DSM-derived shade.

District	Date	Solar zenith angle (°)	Solar azimuth angle (°)	View zenith angle (°)	Accuracy
Ground photo					
Bonham Road	2023–02–06	48.0	220.3	–	–
HKU Campus	2023–02–11	37.4	196.5	–	–
Google Earth imagery					
Central and Western	2022–07–24	18.1	93.8	7.1	–
Yau Tsim Mong	2022–07–24	18.1	93.8	7.1	–
Victoria Peak	2022–07–24	18.1	93.8	7.1	–
Lion Rock	2022–07–24	18.1	93.8	7.1	–
PlanetScope imagery					
Central and Western	2020–10–10	33.0	149.4	0.9	0.76
Central and Western	2020–05–04	24.7	100.0	0.9	0.83
East	2020–10–09	36.3	139.4	1.0	0.78
East	2020–12–02	47.2	158.2	1.0	0.73
Kowloon City	2020–04–28	25.0	104.3	0.1	0.81
Kowloon City	2020–12–06	52.9	145.9	1.0	0.73
Kwun Tong	2020–11–01	45.6	141.3	1.0	0.75
Kwun Tong	2020–04–28	25.0	104.3	0.1	0.85
Sha Tin	2020–12–06	53.0	146.0	1.0	0.66
Sha Tin	2020–04–28	25.0	104.5	0.1	0.83
Sham Shui Po	2020–01–08	52.2	146.9	1.0	0.68
Sham Shui Po	2020–04–28	25.0	104.3	0.1	0.76
Wan Chai	2020–01–08	52.1	146.9	1.0	0.73
Wan Chai	2020–10–09	36.3	139.4	1.0	0.76
Wong Tai Sin	2020–12–06	53.0	146.0	1.0	0.68
Wong Tai Sin	2020–10–09	36.3	139.5	1.0	0.78
Yau Tsim Mong	2020–04–28	25.0	104.3	0.1	0.84
Yau Tsim Mong	2020–12–06	52.9	145.9	1.0	0.70
Yuen Long	2020–10–10	33.1	149.5	0.9	0.78
Yuen Long	2020–10–11	37.0	140.4	1.0	0.70

2.3.3. High-resolution satellite data

Two high-resolution satellite datasets, Google Earth imagery data and PlanetScope data, were used to assess the accuracy of the generated shade data (Table 1). The Google Earth satellite data is obtained from the DigitalGlobe WorldView-3 commercial imaging satellite, which has a spatial resolution of 0.5 m. The latest Google Earth imagery available in July 2022 over two urban areas (Central and Western and Yau Tsim Mong districts) and two natural areas (Victoria Peak and Lion Rock mountains) were used as a reference for visual assessment. As the acquisition time of the satellite data for solar geometry calculation was not provided by Google Earth, this auxiliary information was extracted from the original WorldView-3 imagery available at Maxar Technologies Inc. (https://discover.maxar.com).

To quantitatively evaluate the accuracy of the DSM-derived shade, PlanetScope satellite data with a resolution of 3 m was used. Planet Lab Inc. operates over 180 PlanetScope Dove CubeSats, which have provided daily worldwide surface reflectance observations since 2016. The PlanetScope satellite data can be accessed through a research and education license at https://www.planet.com/. Ten administrative districts with varying urban building density gradients were selected as validation sites, including Yuen Long, Sha Tin, Sham Shui Po, Yau Tsim Mong, Kowloon City, Wong Tai Sin, Kwun Tong, Central and Western, Wan Chai, and Eastern (Fig. 2). The orthorectified, level 3B analytic surface reflectance product for these sites in 2020 were downloaded using a low cloud cover threshold (<10 %) and satellite viewing geometry (<1.0°). For each validation site, two images were downloaded, resulting in a total of 20 PlanetScope surface reflectance images used in this study.

2.4. Urban shade

2.4.1. DSM-based ray-tracing approach

A semi-analytical ray-tracing approach (Dozier et al. 1990) was adopted to calculate the horizon angle (i.e., the maximum zenith angle that can be sunlit by solar at a specific azimuth angle and defined by the angle from the zenith to the horizon, Fig. 3) from DSM data. This approach is cost-effective and widely used in the 3-D topographic morphology analysis (Wu et al. 2018) and solar radiation modeling (Steger et al. 2022). This ray-tracing approach involves three main steps:

Step 1: The two-dimensional DSM elevation image is rotated to the solar direction by setting solar azimuth angle as the North. This rotation allows us to simplify the 3-D shade problem into a 1-D equivalent.

Step 2: For each column of the rotated 1-D grid, the elevation array can be extracted and listed as a stack sequence: $Z_1, Z_2, \ldots, Z_N$ (Fig. 4). According to the solar radiative transfer process, the target point i can only be blocked by the point j in its forward direction (i.e., $j = i + 1, \ldots, N$). Two arrays were defined to store the horizon angle (*Hor*) and the associated horizon locations (i.e., the highest neighboring point that will cast a shadow on the target point; *Horp*). The slope function is defined to calculate the relative zenith angle between two points. With these arrays and functions, the horizon angle can be computed from the stack of elevation array using the following sub-steps.

1) Horp $[N] = P_N$.
2) Given point i, if its elevation is higher than any other points in its front ($Z_i > Z_j$ for all $i < j < N$), Horp $[i] = P_i$. Otherwise, the algorithm searches for the farthest and highest point j that has the largest relative zenith angle with target point i (maximum SlopeItoJ), and then Horp $[i] = P_j$.

To speed up the process of finding the farthest and highest point j in the above sub-step 2), a recursive strategy is proposed (Dozier et al. 1990). The relative zenith angle from target point i to point j (SlopeItoJ) and that from target point i and point j's horizon (SlopeItoHorpJ) are compared in two cases:

a) SlopeItoJ > SlopeItoHorpJ (Fig. 4**a**), point j obstructs all points in its front so that they cannot cast shadows on target i, i.e., Horp $[i] = P_j$ and Hor $[i]$ = slope (p_i, p_j).
b) SlopeItoJ ≤ SlopeItoHorpJ (Fig. 4**b**), all points between point j and its horizon point k have a smaller relative zenith angle than SlopeItoHorpJ, i.e., Horp $[i] = P_k$ and Hor $[i]$ = slope (p_i, p_k).

Using this recursive strategy, this algorithm can improve the algorithm efficiency from the original order N^2 to the order N (Dozier et al. 1990).

Step 3: The calculated horizon angle along the solar azimuth geometry is re-rotated to the original direction of DSM.

2.4.2. Calculation of urban shade and sunlight hour

Based on the ray-tracing approach described above, the accurate calculation of horizon angle is crucial for quantifying urban shade. The proposed method for determining the horizon angle involves two steps. First, the solar geometry was calculated, including the solar zenith angle and solar azimuth angle, at a 10-minute interval from 06:00 to 18:00 throughout the year (Szokolay, 1996). Analysis showed that in Hong Kong, the solar zenith angle ranged from 0° to 90° (daytime), and the solar azimuth angle ranged from 40° to 320° (Fig. 5). Second, the azimuth angle range was divided into 57 bins at a 5° interval (40°, 45°, …, 320°) based on the annual cycle of solar geometry. For each azimuth angle bin, the corresponding horizon angles were computed and stored

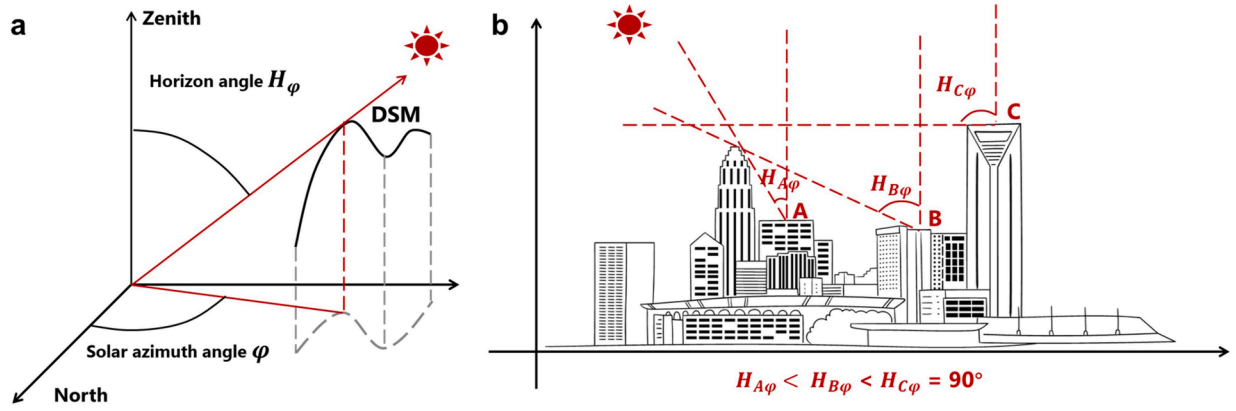

Fig. 3. Horizon angle in shade calculation with **(a)** schematic diagram of horizon angle from DSM data and **(b)** three examples of horizon angles in the urban environment. H_φ is the horizon angle at the azimuth angle φ.

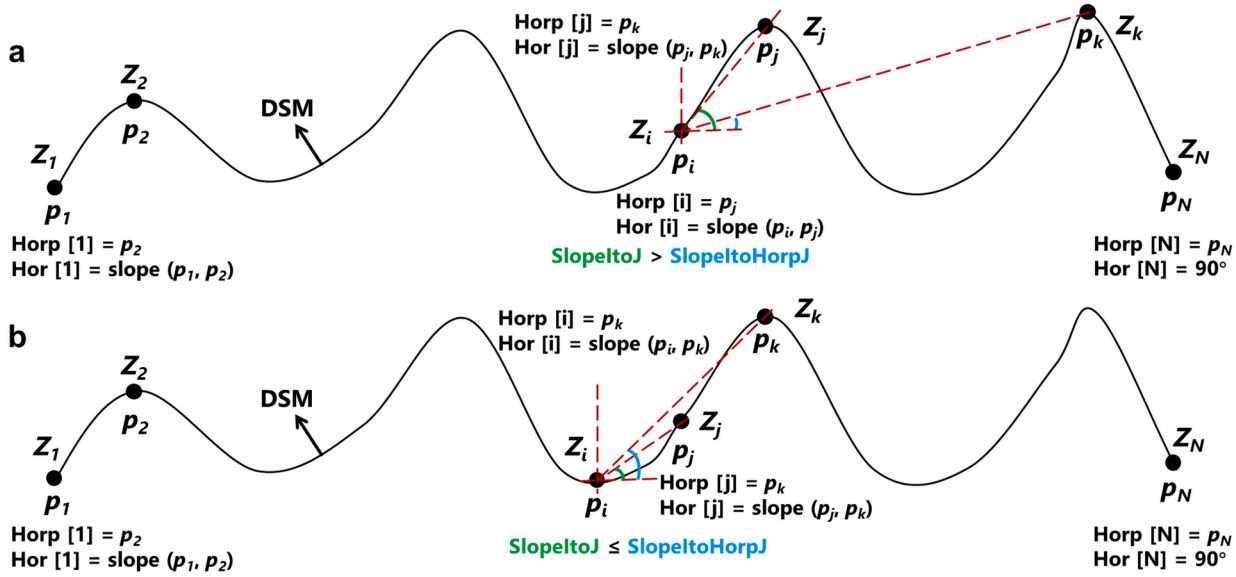

Fig. 4. Recursive strategy for the calculation of horizon angle (Hor) and the associated horizon location (Horp) by comparing the relative zenith angle from target point i to point j (SlopeItoJ) with that from target point i and point j's horizon (SlopeItoHorpJ), including **(a)** SlopeItoJ $>$ SlopeItoHorpJ and **(b)** SlopeItoJ $\leq$ SlopeItoHorpJ. Slope is the function for the calculation of the relative zenith angle between two random points in the elevation array. P_i and Z_i denote the position and elevation of target point i, respectively; N refers to the elevation array length.

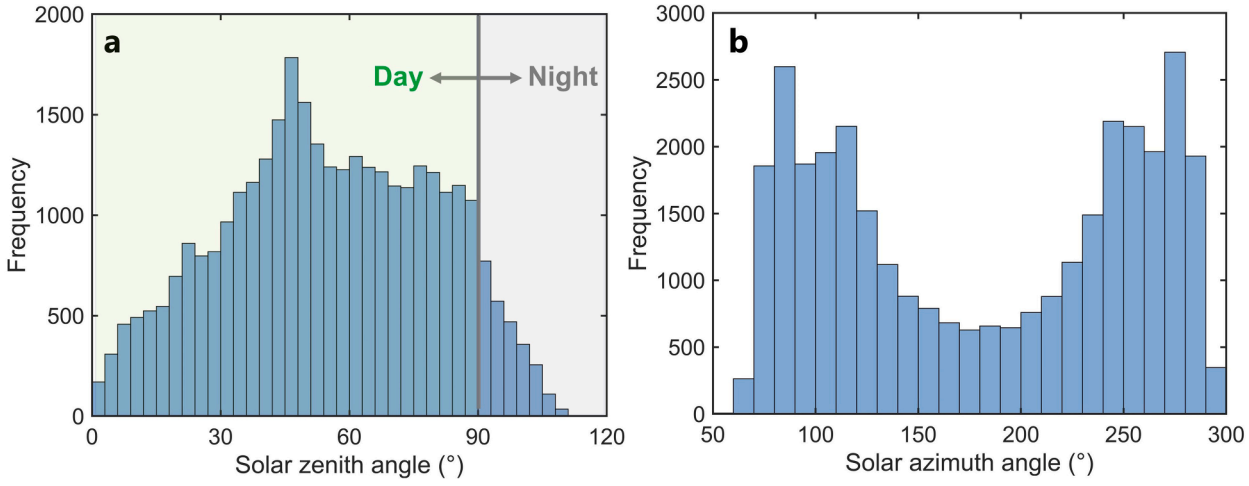

Fig. 5. Histograms of **(a)** solar zenith and **(b)** solar azimuth angle in Hong Kong for a one-year cycle. Solar zenith angles that are lower and larger than 90° in **(a)** refer to daytime and nighttime, respectively.

them in look-up tables (LUTs). Sensitivity analysis reveals that 5° interval is appropriate for the calculation of horizontal angle LUTs (**Fig. S1**).

Using these LUTs, urban shade can be determined for any given solar geometry. The LUT that most closely matched the solar azimuth angle was located and used to calculate the shade. For each pixel, if its horizon angle is smaller than the solar zenith angle, it will be considered as shaded; otherwise, it is sunlit. By calculating the shade distribution for all daytime hours, the duration of sunlight can be calculated for each day throughout the year.

2.5. Accuracy validation of urban shade

With the multi-source shade references, the accuracy of the urban shade estimates was validated through both visual and quantitative assessments. Ground-based photo references and Google Earth imagery were used for visual evaluations due to their limited spatial extent and solar geometry variation. PlanetScope satellite datasets were used for quantitative assessment because of their large variations in solar position, with the solar zenith and azimuth angles ranging between 24.7°-53.0° and 100.0°-158.2°, respectively.

The support vector machine (SVM), one of the widely used supervised machine learning approaches (Mountrakis et al. 2011), was adopted to generate shade references from PlanetScope data. We manually labeled shade and non-shade training samples (> 500 pixels for each class) for each PlanetScope imagery and then trained the SVM classification algorithm using these labeled samples and classified the entire imagery into a binary map of shade and non-shade. To evaluate the accuracy of the shade classification derived from PlanetScope. 20 random sample points for each PlanetScope image were generated and visually assessed. Validation results confirm the reliability of PlanetScope-derived shade as a validation reference, with an overall accuracy of 0.94 (**Table. S1**). Based on PlanetScope-derived reference, the 0.5-m resolution DSM-derived shade estimates were reprojected to the 3-m resolution for comparison. The fraction of correct pixel predictions over the whole imagery was defined as the accuracy metric for validation purposes (Eq. (1)). As the shades of nature covers (e.g., tree canopy and grassland) are difficult to detect from PlanetScope data, we compared PlanetScope and DSM-derived shades only over urban built-up areas by masking out the nature vegetations using the land utilization map from the Planning Department in Hong Kong (https://www.pland.gov.hk/pland_en/info_serv/open_data/landu/index.html).

$$Accuracy = \frac{N_{shade} + N_{sunlit}}{N_{all}} \quad (1)$$

where N_{shade} and N_{sunlit} represent the number of shaded and sunlit pair-pixels between PlanetScope and DSM-derived classification maps, respectively. N_{all} is the total pixel number.

2.6. Spatiotemporal dynamics of urban shade

Four regions over the Wan Chai, Kowloon City, Yuen Long, and Tai Po districts, which share different 3-D urban morphology gradients, were selected to explore the spatial patterns of urban shade at 9:00 and investigate the associated diurnal variations from 6:00 to 18:00 with one-hour interval on July 1, 2020. To further quantify the controlling effects of solar geometry on the spatiotemporal variations of urban shade, we compared a suite of shade landscape metrics (a total of 9 landscape configuration metrics calculated from the shade and non-shade binary classification map, Table 2) with solar zenith angle and solar azimuth angle. Solar geometry for four selected regions was calculated at local solar noon (12:00) on each day in 2020. Using the horizon angle LUTs, the shade maps were calculated and then quantified the associated landscape metrics (Hesselbarth et al. 2019). Finally, the associations between solar geometry and shade landscape metrics were evaluated using four commonly used fitting equations (i.e., polynomial, exponential, power exponential, and logarithmic functions).

Table 2
Landscape metrics used for characterizing shade landscape configurations (Hesselbarth et al. 2019).

Metric	Formula	Description	Unit	Range
Aggregation index (AI)	$AI = \frac{g_{ii}}{max \rightarrow g_{ii}} \times 100$	g_{ii} = Number of like adjacencies between pixels of patch type i based on the double count method. $max \rightarrow g_{ii}$ = Maximum number of like adjacencies between pixels of patch type i based on the single-count method	Percentage	0≤AI<100
Landscape division index (LDI)	$LDI = 1 - \sum_{j=1}^{n} \left(\frac{a_{ij}}{A}\right)^2$	α_{ij} = Area (m^2) of patch ij. A = Total number of cells in the landscape.	Proportion	0≤LDI<1
Largest patch index (LPI)	$LPI = \frac{max(a_{ij})}{A} \times 100$	α_{ij} = Area (m^2) of patch ij. A = Total number of cells in the landscape.	Percentage	0 < LPI ≤ 100
Mean perimeter-area ratio (MPAR)	$MPAR = Mean\left(p_{ij}\right)$	p_{ij} = Perimeter of patch ij in terms of number of cell surfaces.	None	MPAR >0
Edge density (ED)	$ED = \frac{\sum_{j=1}^{n} e_{ij}}{A}$	E = Edge length between class i and class j. A = Total number of cells in the landscape.	Meters per hectare	ED > 0
Normalized landscape shape index (NLSI)	$NLSI = \frac{e_i - min\ e_i}{max\ e_i - min\ e_i}$	e_i = Total edge length in cell surfaces. $min/max\ e_i$ = Minimum/ maximum total edge length in cell surfaces.	None	0≤NLSI≤1
Number of patches (NP)	$NP = n_i$	n_i = Total number of patches in the landscape of patch type i.	None	NP ≥ 1
Patch density (PD)	$PD = \frac{n_i}{A} \times 10,000 \times 100$	n_i = Total number of patches in the landscape of patch type i. A = Total number of cells in the landscape.	Number per 100 hectares	0<PD≤1
Total edge (TE)	$TE = \sum_{j=1}^{n} e_{ij}$	e_{ij} = Edge length between class i and class j.	Meters	TE ≥0

2.7. Spatiotemporal dynamics of sunlight hour

Based on the pixel-level shade datasets, the sunlight hours were mapped across the entirety of Hong Kong by accumulating pixel-level shade information during the daytime and subtracting it from the total daylength. With this sunlight hour map, the average sunlight hours were aggregated and computed for each administrative district in Hong Kong on July 1, 2020. The differences in sunlight hours among local climate

zones (LCZs) types were then explored by combing sunlight hour and the LCZ maps from the 100-m global raster map (Demuzere et al. 2022). The association analysis between sunlight hour and surface elevation was conducted to decipher the controlling effects of 3-D morphology on sunlight duration. Lastly, the seasonal patterns of sunlight hours among 18 administrative districts in 2020 were extracted and compared.

3. Results

3.1. Accuracy of DSM-derived shade map

The accuracy validation of the DSM-derived shade dataset was conducted by using three references: ground-based photo references, Google Earth imagery, and PlanetScope satellite data. Results showed that the DSM-derived shade accurately captures the solar blocking effects of the 3-D built environment (Fig. 6). For instance, the sun illuminated the Hong Kong Island along the Southwest-Northeast direction at 14:37 on February 6 (white regions in Fig. 6**a and b**). However, due to the blocking effects of Ying Yin Mansion and Ning Yeung Terrace, most parts of Good View Court were shaded. On the other hand, the roadside of Ning Yeung Terrace was sunlit, resulting in a section of Good View Court at the road corner being illuminated by the sun. These simulated shading patterns are highly consistent with the ground photo at a local scene view (Fig. 6**c**). Similarly, both the simulated shade map and ground photo showed that the central part of Sun Yat Sen Place at HKU campus was shaded, resulting from the sunlight interception by the HKU main Library and Knowles Building (Fig. 6**d–f**). Interestingly, the DSM data can also replicate the casting shadow of individual tree-crown on the ground and self-shadows of the Knowles Building (Fig. 6**e** and 6**f**).

The DSM-derived shade is assessed by high-resolution Google Earth RGB imagery (Fig. 7). The DSM data captures different shading effects over urban areas, including the casting shadows of tall buildings, pedestrian bridges and 3-D road networks onto the ground, as well as the self-shadows on the rooftops (Fig. 7**a–d**). Moreover, the DSM data provides insight into the sunlight conditions of tree canopies in two distinct natural landscapes (Fig. 7**e–h**), which show contrasting spatial patterns. Victoria Peak shows a more diverse canopy structure over central regions with a larger proportion of canopy shadows (Fig. 7**e and f**). By contrast, the Lion Rock landscape exhibits greater homogeneity in the margin regions, together with more canopy shadows (Fig. 7**g and h**). These results demonstrate the potential of shadow maps in inferring the complex 3-D complex morphology of both urban and natural environments.

The accuracy of DSM-derived shade is evaluated quantitatively at a 3-m resolution by satellite maps extracted from PlanetScope data using the SVM classification approach. The evaluation shows a high level of agreement ranging from 0.66 to 0.85 (Table 1). Visually, the coarser spatial resolution of PlanetScope satellite imagery limits its ability to detect small targets such as trees and low buildings, resulting in an over-smooth spatial pattern of shade, albeit it is able to detect shade of large targets such as tall buildings (Fig. 8). In contrast, the high-resolution DSM data provides much more spatial details, such as long-tailed building shade and scattered canopy shade, thereby offering greater informative maps.

3.2. Spatial and diurnal patterns of urban shade

The 0.5-m resolution DSM map allows for exploring spatial heterogeneity of urban shade at the individual building level (Fig. 9). Results show the distribution of urban shade is closely related to the 3-D morphology of buildings, including size, shape, height, and density. For instance, tall buildings cast larger shade footprints than lower buildings or vegetation covers. Moreover, larger and high-density buildings tend to induce a greater proportion of shade than sparsely distributed buildings. Overall, at the same morning time of day, the mean shade fractions are increasing with building density. The Wan Chai district has the highest shade proportion (0.54) and building density, followed by the Kowloon City (0.46), Yuen Long (0.39), and Tai Po (0.29) districts.

The fraction of urban shade exhibits significant diurnal variation during the daytime (Fig. 10 **and S2-S4**). Using the Wan Chai district as an example, in the early morning, when the sun has a large zenith angle,

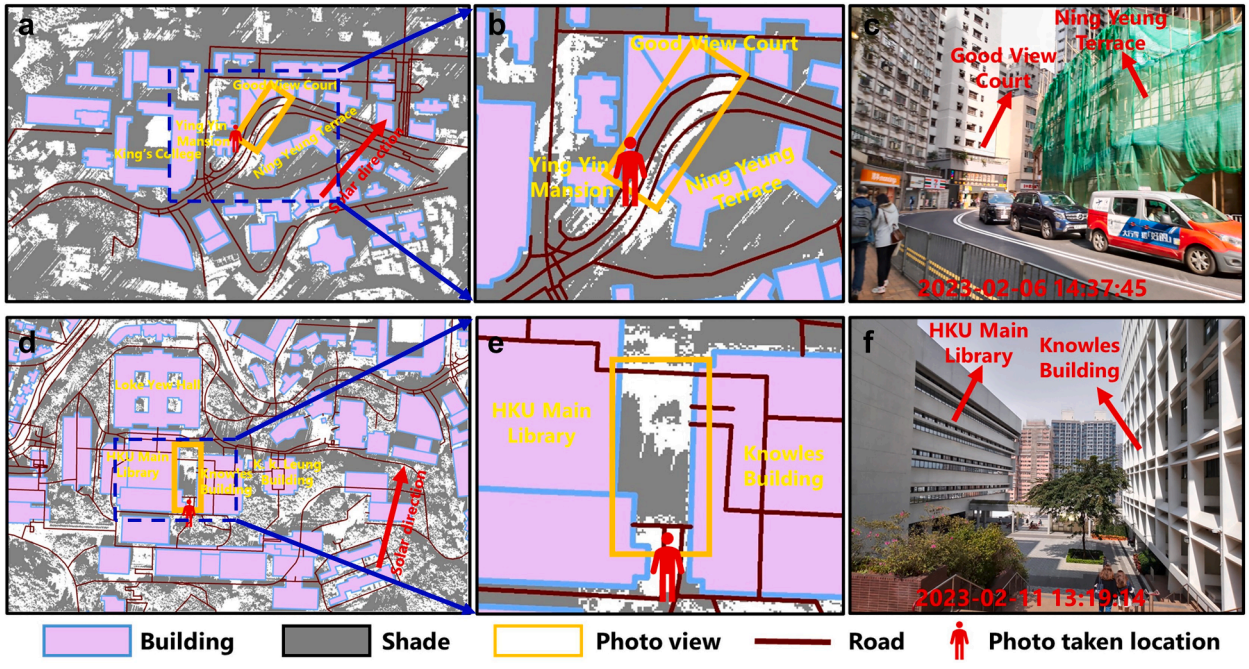

Fig. 6. Visual comparisons between DSM-derived shades and ground-based photo references at **(a-c)** Bonham Road and **(d-f)** University of Hong Kong (HKU) Campus. **(a)** and **(d)** are the overviews of the calculated shade overlaid on building footprints and road layers, with gray and white representing shaded and non-shaded areas, respectively. **(b)** and **(e)** are the magnified views of the shaded areas within the blue dashed rectangles in **(a)** and **(d)**, respectively. **(c)** and **(f)** are the corresponding ground photos. The building footprints and road layers are extracted from the OpenStreetMap dataset (https://www.openstreetmap.org).

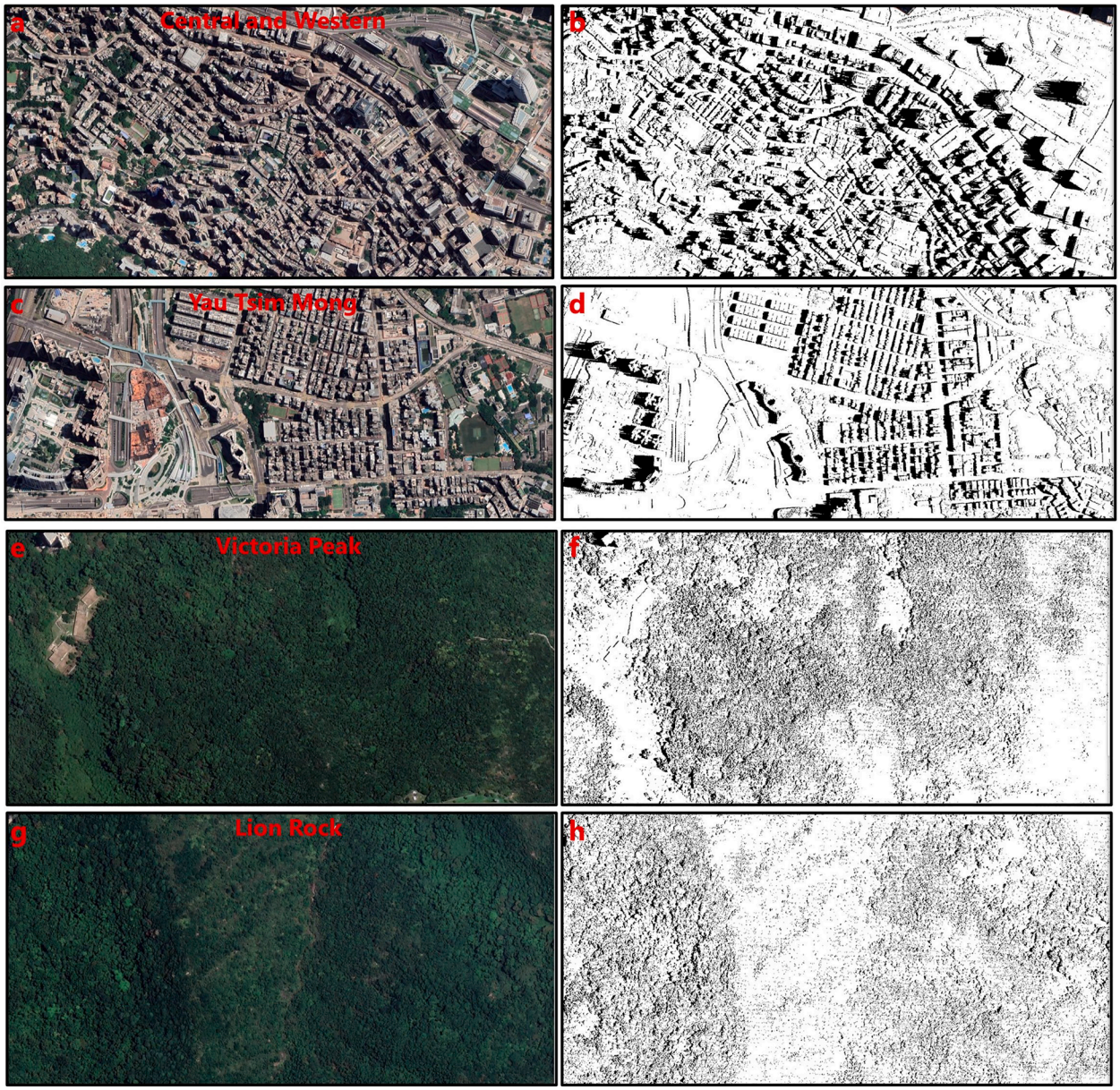

Fig. 7. Visual comparisons between DSM-derived shades and Google Earth RGB imagery over **(a-d)** two urban areas in Central and Western and Yau Tsim Mong districts and **(e-h)** two forest landscapes in Victoria Peak and Lion Rock mountains. **(a, c, e,** and **g)** are Google Earth RGB imageries acquired at 11:10:00, July 24, 2022. **(b, d, f,** and **h)** are the associated shade maps, with dark and white regions presenting shaded and sunlit regions, respectively.

a considerable portion of the ground is shaded. As the sun rises, the solar zenith angle decreases, which increases the sunlit surface area, reaching the peak at local noon time. In the afternoon, the solar zenith angle increases again until sunset, resulting in an increased proportion of urban shade. This diurnal cycle is quantitatively characterized by the symmetric change of mean shade fraction within the day (Fig. 10**k**). However, despite the symmetric shade fraction throughout the day, the direction of shade significantly changes from morning to afternoon as the solar azimuth angle shifts from the easting direction to the westing direction.

3.3. Controls of solar geometry on shade landscape configuration

The diurnal and seasonal patterns of urban shade are predominantly controlled by the changes in solar geometry (i.e., solar zenith and azimuth angles), resulting in large variations of shade landscapes. To quantify these controls, the relationships between solar geometry and different shade landscape metrics were examined (Fig. 11). Solar zenith angle is strongly associated with two types of shade landscape metrics. Aggregation metrics, such as the largest patch index, mean perimeter-area ratio, aggregation index, and normalized landscape shape metrics, decrease with increasing solar zenith angle (Fig. 11**a–d**). Conversely, fragmentation metrics, such as edge density, total edge, landscape division index, patch density, and patch number metrics, show an increase with increasing solar zenith angle (Fig. 11**e-i**), indicating that higher solar zenith angles create more shade patches and edges. Interestingly, different fitting functions were observed with each type of association. For example, the largest patch index, mean perimeter-area ratio, and aggregation index show a linear decrease with solar zenith angle, while the normalized landscape shape index demonstrates a power decrease. Solar azimuth angle exhibits similar associations with shade landscape metrics, albeit with lower agreement (Fig. 12).

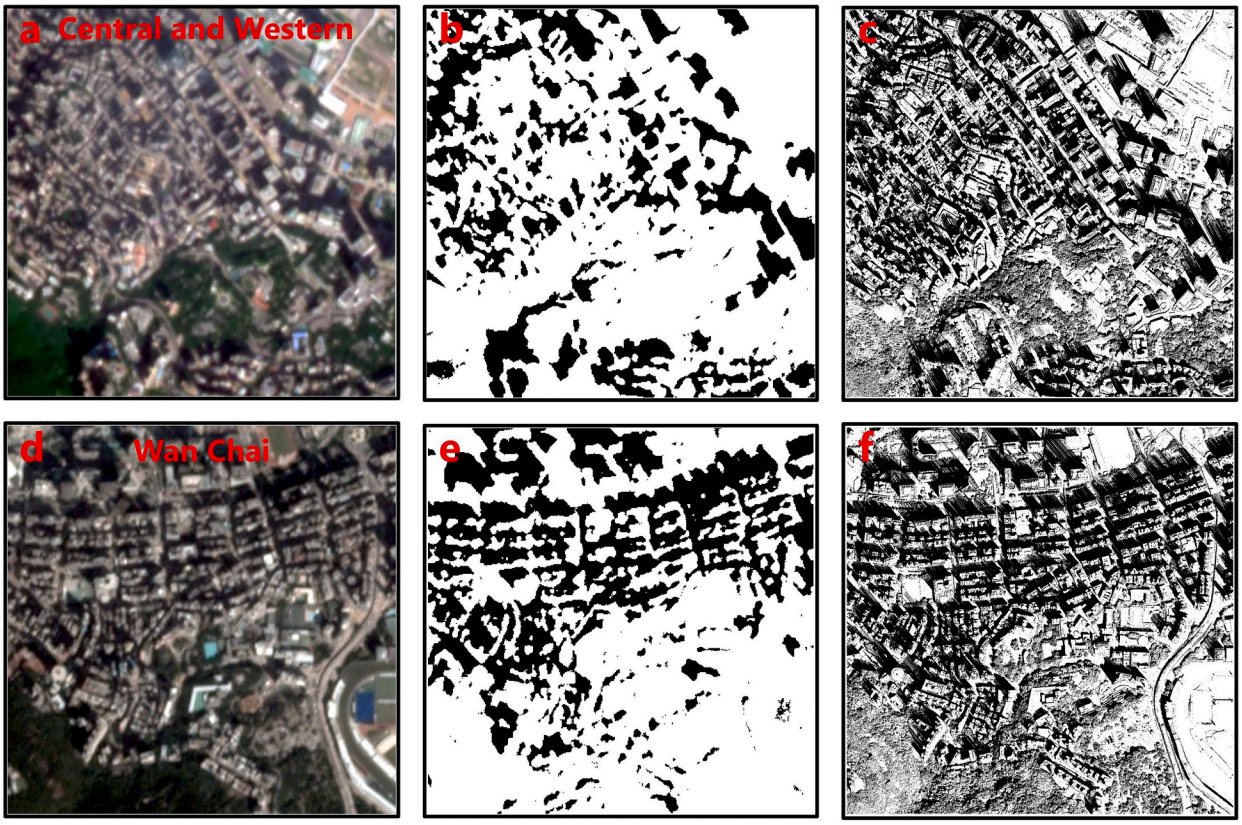

Fig. 8. Visual comparisons between DSM-derived shades and PlanetScope satellite imagery over two districts: **(a-c)** Central and Western and **(d-f)** Wan Chai. **(a)** and **(d)** are PlanetScope RGB imageries acquired on October 10, 2020, at 11:05:53 and October 9, 2020, at 10:39:10, respectively. **(b)** and **(e)** are the PlanetScope-derived shade map using the SVM classification approach. **(c)** and **(f)** are the DSM-derived shade maps. In the shade maps, dark and white regions represent shaded and sunlit areas, respectively.

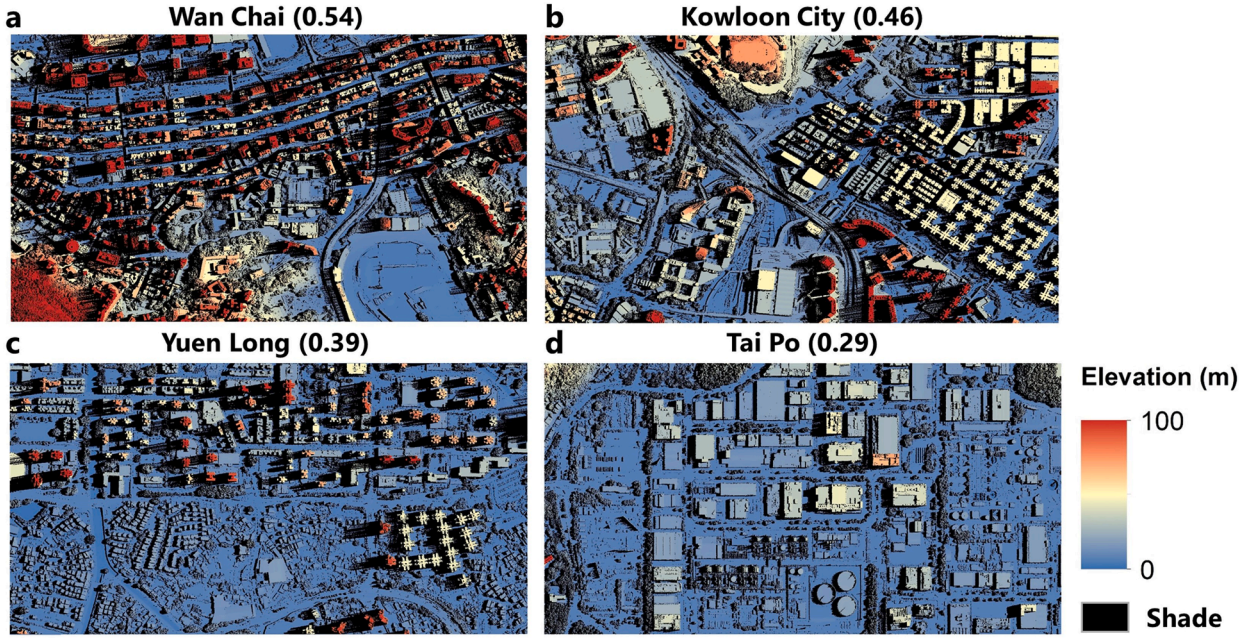

Fig. 9. Spatial distribution of urban shade in four districts at 9:00 on July 1, 2020: **(a)** Wan Chai, **(b)** Kowloon City, **(c)** Yuen Long, and **(d)** Tai Po. The mean shade fractions for each district are displayed in parentheses on the subplot titles.

3.4. Spatial and seasonal patterns of sunlight hour

The spatiotemporal distribution of sunlight hours was analyzed across pixel-level grids, administrative districts, LCZ types, and seasons. Compared to human settlement areas, natural areas and impervious surfaces located near the coast, such as the Northwest (e.g., Mai Po

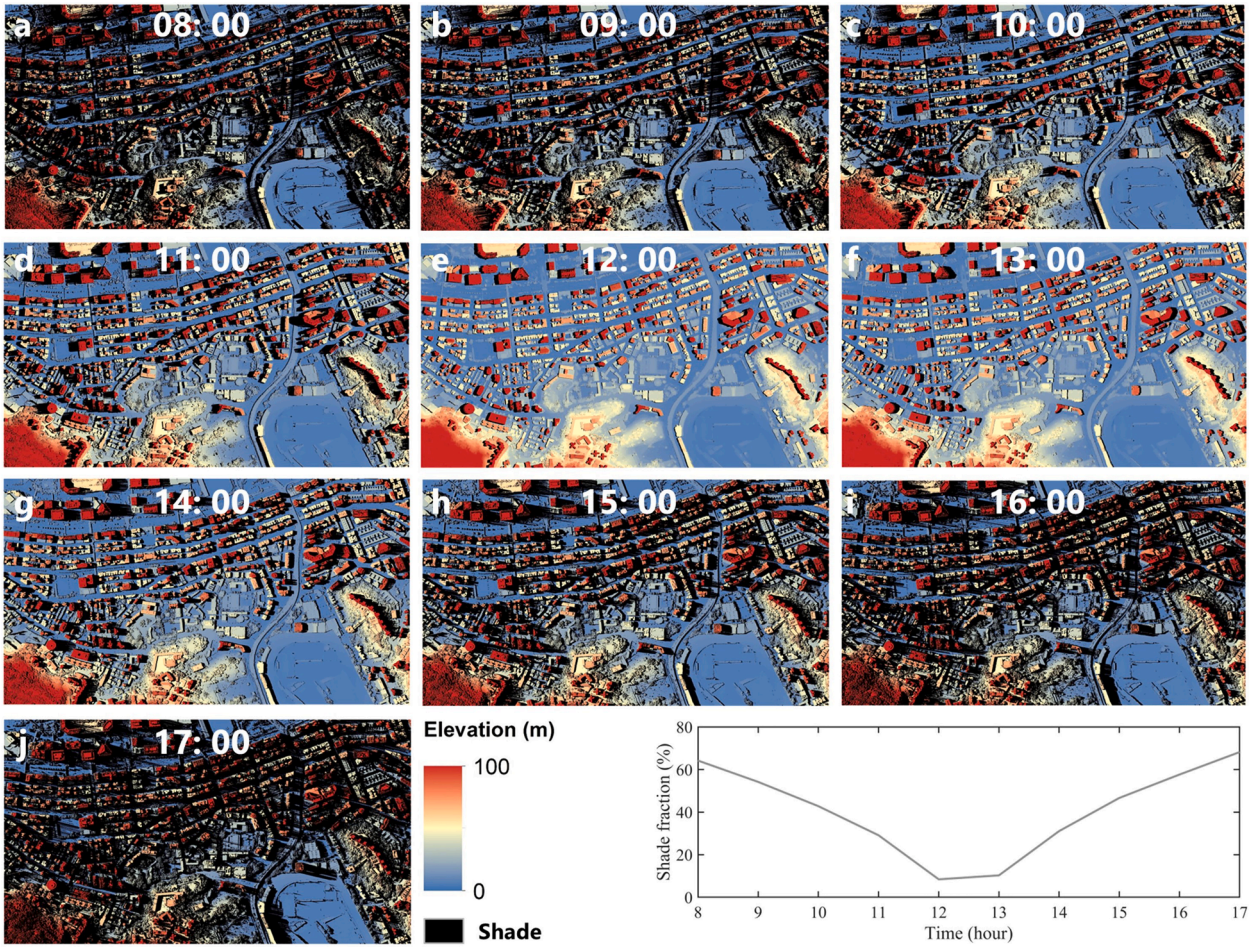

Fig. 10. Diurnal variations of urban shades in Wan Chai district on July 1, 2020, with a one-hour interval from **(a)** 8:00, **(b)** 9:00, **(c)** 10:00, **(d)** 11:00, **(e)** 12:00, **(f)** 13: 00, **(g)** 14: 00, **(h)** 15:00, **(i)** 16:00, to **(j)** 17:00. **(k)** is the associated diurnal variation of mean shade fraction.

Nature Reserve), Southwest (e.g., Hong Kong International Airport), and Southeast (e.g., Po Toi Island) regions, experience longer sunlight hours (Fig. 13). By administrative district, Islands, Yuen Long, and Sai Kung have the longest mean sunlight hours of 9.5, 9.0, and 8.3, respectively, whereas Wan Chai, Central and Western, and Eastern experienced the shortest mean sunlight hours of 6.6, 6.9, and 6.8, respectively.

As shown in Fig. 14, sunlight hours vary across different LCZ types. Natural LCZ types, such as scatter trees, receive longer sunlight hours compared to the built-up LCZ types, like heavy industry. Moreover, compact and open LCZ types receive shorter sunlight hours than other built types. Interestingly, within the same compact or open LCZ types, lowrise structures experience longer sunlight hours than midrise and highrise structures, highlighting that building height plays a crucial role in determining sunlight hours in built environment. These findings are further supported by the negative correlation between sunlight hours and surface elevation (Fig.14b).

Sunlight hour shows similar seasonal patterns across 18 administrative districts, although there are large variations (Fig. 15). It increases from winter to spring, reaches the peak value in summer, and then decreases from summer to winter. On average, the sunlight hour in Hong Kong ranges from 4.4 to 8.0 h per day over the course of a year.

4. Discussion

4.1. Urban shade estimation

This study proposed a novel protocol for mapping city urban shade by combing LUT-based ray-tracing approach with Google Earth Engine (GEE) cloud computing technology, and fine-resolution LiDAR-derived DSM data. Compared with previous approaches that rely on Google Street View panoramas or 3-D city models (X. Li and Ratti, 2018; X. Li et al. 2018), this protocol has three major advantages regarding approach theory and practical application. First, the ray-tracing approach is grounded in solid physical principles and can mimic complex interactions between solar radiation and the 3-D built environment (Compagnon, 2004). Besides the self-shadows (i.e., the shade generated by the target itself), this approach can also account for the casting shadow effects from higher neighboring objects by using a buffer size analysis in the horizon angle calculation (Fig. 3**b**). As the maximum surface elevation in Hong Kong is around 960 m, a 1000-m buffer size to account for the maximum neighboring effect were used. Second, the proposed framework adopts horizon angles as a measuring proxy of shade, which is an intrinsic characteristic of urban structures and is independent of the varying solar geometry that requires substantial computational resources. This approach built the LUTs of horizon angle and further empowered by the GEE cloud computing platform to minimize time cost, allowing citywide shade mapping in just a few seconds, significantly faster than the traditional ray-tracing approach deployed on GIS platforms. Computational analysis revealed that it only takes a total of 98 h to create the horizontal angle LUTs with a 5° interval for the solar azimuth angle for the entire Hong Kong, using a personal desktop (e.g., 8.00 GB RAM, i5–10,505 CPU @ 3.20GHz 3.19 GHz). Moreover, these pre-built LUTs of horizontal angle can feasibly be adopted for analyzing many other significant urban morphology parameters, such as shade, sunshine time, and sky view factor. Third, in contrast to Google Street View panoramas or 3-D city datasets with limited local views, this

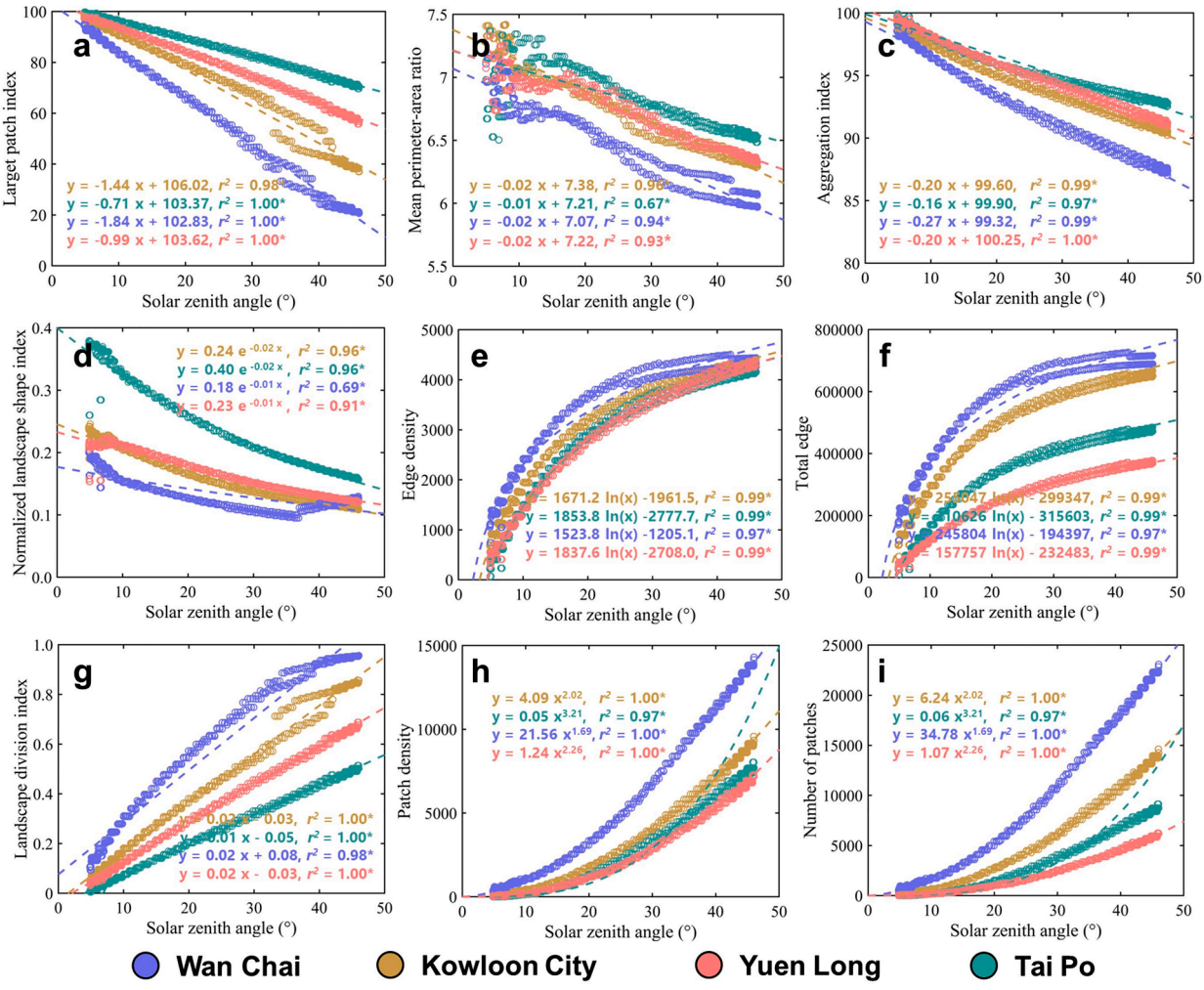

Fig. 11. Associations between solar zenith angle and shade landscape metrics, including **(a)** largest patch index, **(b)** mean perimeter-area ratio, **(c)** aggregation index, **(d)** normalized landscape shape index, **(e)** edge density, **(f)** total edge, **(g)** landscape division index, **(h)** patch density, and **(i)** number of patches.

approach allows for the mapping of seamless shade conditions at the pixel level over large scales. With the increasing availability of high-resolution LiDAR products, such as the 3-D Elevation Program (3DEP) led by the United States Geological Survey (Stoker and Miller, 2022), Copernicus EEA-10 Digital Elevation Model (Cenci et al. 2022), and the forthcoming launch of 3D Optical Constellation (CO3D) satellite mission (Lebègue et al., 2020), the proposed protocol will offer a unique opportunity to quantify and analyze urban shade distributions within the individual city and across cities globally.

4.2. Urban shade spatiotemporal dynamics and landscape configurations

Urban shade exhibits a strong spatiotemporal variability, resulting from the complex interplay between 3-D urban structure and solar geometry. Natural vegetation covers, such as trees and shrubs, typically have smaller shading footprints compared to built-up areas like buildings, as shown in Fig. 9. The height, shape, size, orientation, and aggregation of 3-D buildings are crucial factors in casting self-shadows, with tall and more densely grouped buildings casting greater shadows than lower and more dispersed ones (Fig. 9). Further research is required to understand how building shape and size affect shadow casting. Nonetheless, it is expected that the larger effective cross-sectional building areas aligned with the direction of solar illumination will create more cast shadows. The diurnal dynamic of urban shade is influenced by shifting solar geometry, with a consistent daily rhythm of the solar zenith angle and shade fraction in a "U-shape" pattern. The association between solar geometries and shade landscape metrics highlights the controls from the solar position on spatial arrangements of urban shade. The increase of solar zenith and azimuth angles will simultaneously cause larger shade patches (Figs. 11 **and** 12). Importantly, the solar zenith angle exhibits a stronger control over urban shade landscape than the solar azimuth angle.

The cumulative effects of urban shade led to varying sunlight durations across space at the pixel-level grid, administrative district, and LCZ type. Spatially, the pixel-level sunlight hour in Hong Kong exhibits a "bowl-like" distribution, where the central regions experience much shorter sunlight hours than the marginal regions, especially for near-coastal areas (Fig. 13**a**). This unique spatial pattern results from the combined effects of physical topography, 3-D built morphology, and coastal environment. The regions in the Northwest, Southwest, and Southeast with large sunlight hours are situated in flat topography areas and surrounded by open or continental seas without neighboring blocking effects. Conversely, the high-density built environments in the central regions (such as Wan Chai district) obstruct solar radiation and reduce sunlight hours. Statistical analysis of sunlight hours among administrative districts reveals that the three most urbanized areas—Wan Chai, Central and Western, and Eastern—have the shortest sunlight durations, with approximately 1.4–2.9 fewer hours than the more natural districts of Islands, Yuen Long, and Sai Kung. Moreover, the combination of built environment and land cover types results in different sunlight hours across LCZ types, with the compact high-rise LCZ type exhibiting the shortest sunlit time (around 6.1 h) (Fig. 14**a**).

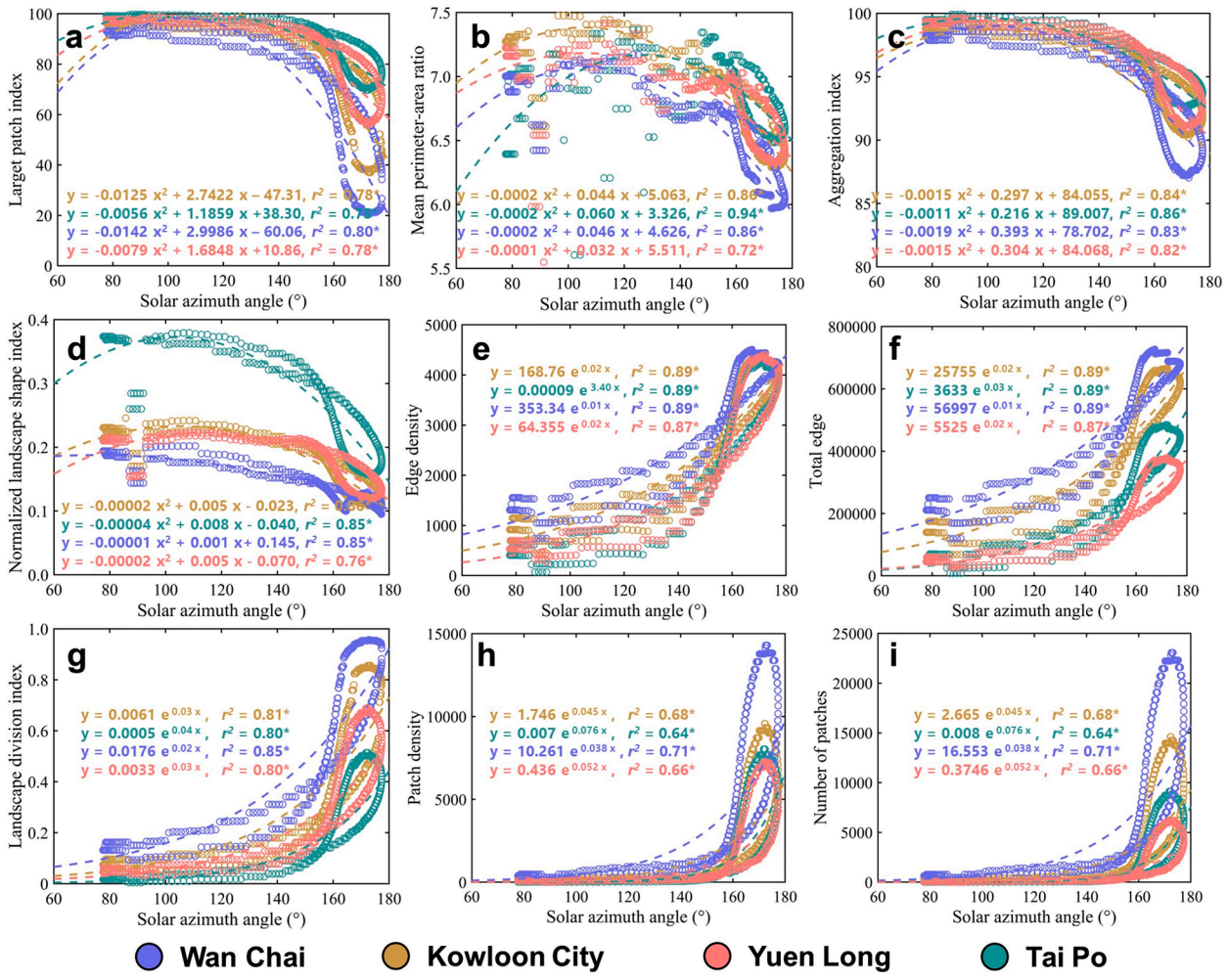

Fig. 12. Associations between solar azimuth angle and shade landscape metrics, including **(a)** largest patch index, **(b)** mean perimeter-area ratio, **(c)** aggregation index, **(d)** normalized landscape shape index, **(e)** edge density, **(f)** total edge, **(g)** landscape division index, **(h)** patch density, and **(i)** number of patches.

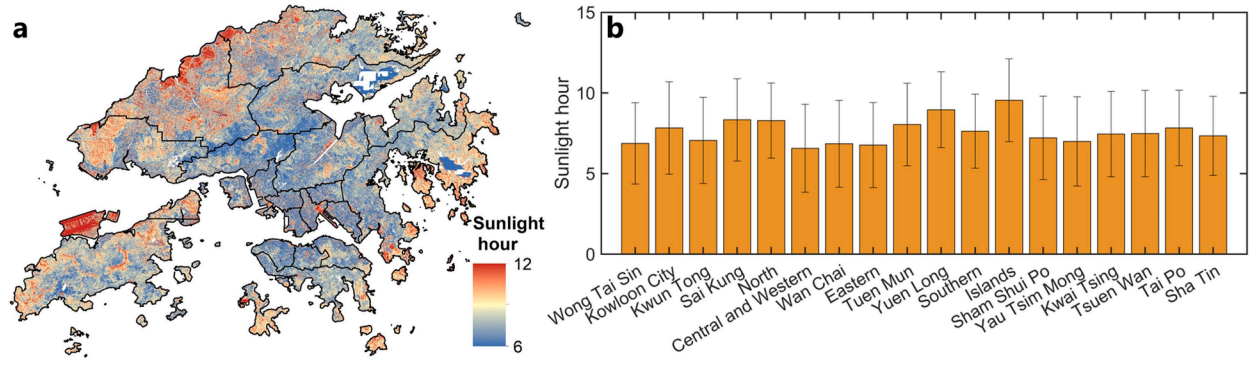

Fig. 13. Spatial pattern of sunlight hours on July 1, 2020, including **(a)** pixel-level map and **(b)** mean sunlight hours over 18 administrative districts.

The strong association between sunlight hours and surface elevation, with a coefficient of determination of $r^2 = 0.27$ ($p < 0.05$), indicates that height significantly influences surface sunshine time. Nevertheless, variations in sunlight hours may also be attributed to other urban morphology metrics that warrant further investigation.

Sunshine time exhibits seasonal dynamics, with a peak sunlight hour in summer and a valley in winter. Notably, this study finds that the total annual sunshine time in Hong Kong ranges from 4 to 8 h (Fig. 15), which is substantially shorter than its physical daytime length of around 11 to 14 h, as the DSM-derived sunshine time considers the impacts of 3-D surface morphology, including topography, buildings, and canopy structure. This finding highlights the importance of considering 3-D urban morphology when assessing solar energy-related activities in urban environments, such as estimating solar energy potential (Calcabrini et al., 2019; Cheng et al. 2020; Zhu et al. 2020).

4.3. Implication of urban shade

Surface cooling is a well-documented benefit of urban shade (Horváthová et al. 2021). However, existing studies on the cooling effect

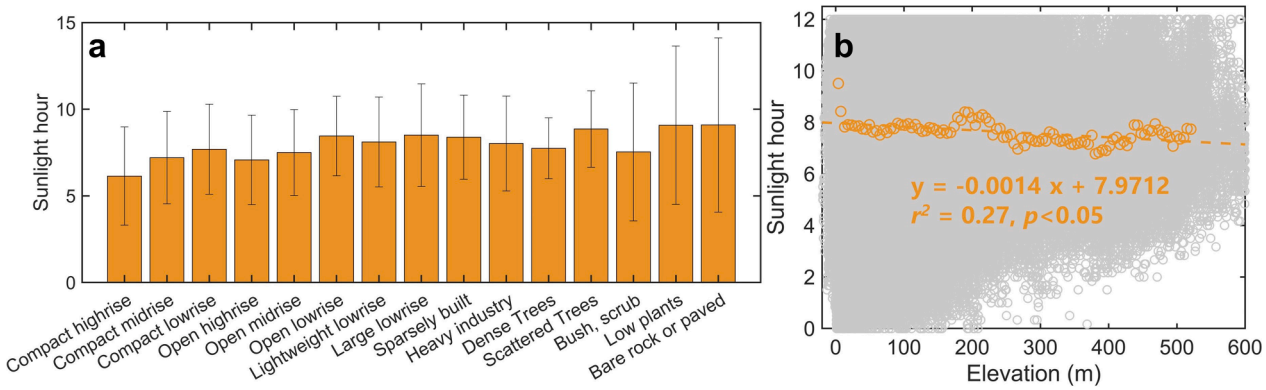

Fig. 14. Controls of urban morphology on sunshine time, including **(a)** mean sunlight hours over different local climate zone (LCZ) types and **(b)** associations between the sunlight hour and surface elevation. The sunlight hour is calculated on July 1, 2020. The orange open circles are bin-averaged elevation and sunlight hour across surface elevation bins with a 1st percentile interval. The dashed orange line represents the linear regression of the binned average values.

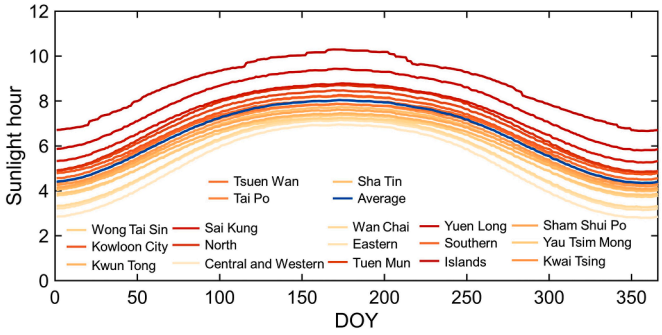

Fig. 15. Seasonal variations of sunlight hours in the 18 administrative districts of Hong Kong throughout 2020.

of tree shades have mainly focused on specific areas (Park et al. 2021; Yu et al. 2020) and have not fully explored the underlying mechanisms on the cooling effects from 3-D tree structure (e.g., tree size, shape, arrangement, and species) and built morphology. The high-resolution spatiotemporal shade datasets generated in this study, along with the diverse tree species and subtropical climate in Hong Kong, offers an optimal urban setting for examining the influence of 3-D landscapes (buildings and trees) on thermal comfort improvement. With a 0.5-m resolution DSM, individual buildings and tree crowns can be accurately segmented for a systematic evaluation of natural and artificial shades on surface cooling. This will facilitate the disentanglement of the physical and physiological cooling effects of vegetation by decoupling the relative contributions of shade and evapotranspiration (Kong et al. 2016; Lachapelle et al. 2023), as well as quantifying the impacts from 3-D building structures (Speak et al. 2020; Wu et al. 2023). Moreover, the cooling effects of shade can be compared across a variety of urbanization gradients, seasons, and extreme climate events (Wang et al. 2019).

Sunlight exposure, which is inversely related to urban shading, plays a crucial role in public health and well-being, contributing to vitamin D synthesis and influencing conditions such as depression and seasonal affective disorder. However, it has often been overlooked in urban planning and design practices (Wu, Chen, An, Lin, & Gong, 2024). This study highlights the impact of 3D urban structures on sunlight availability, emphasizing the need for public awareness concerning the risk of inadequate sunlight exposure in urban settings. The proposed digital twin approach that combines physical modeling, LiDAR observations, and cloud computing platforms, offers a powerful tool to effectively quantify and elucidate potential risks associated with sunlight loss, which can lead to adverse health effects and impact solar power collection through solar PV panels. These observational findings can assist policymakers in managing and planning urban shade and sunlight exposure, adhering to the key principles of supply-demand optimization (Jiao et al. 2021).

4.4. *Limitation and future perspective*

Some limitations in this study should be acknowledged. First, the calculation of shade and sunlight hours only accounts for clear-sky weather conditions and does not consider the confounding effects of cloud cover, fog, and rain. The estimates in this study represent the minimum potential of urban shades. The frequent cloudy and rainy weather in Hong Kong suggest somehow overestimations in sunlight hours (Li et al. 2004). Geostationary satellites with real-time cloud information could be integrated to improve the accuracy of sunlight hour estimation (Letu et al. 2020). Second, this study does not fully consider the 3-D heterogeneous nature of urban shade, such as the vertical distribution of shade within individual buildings or tree crowns. For instance, the upper parts of buildings or tree crowns typically experience longer sunshine duration than their lower counterparts, due to their larger proportion of sky view (Kükenbrink et al. 2021; Rahman et al. 2018). This issue stems from the LiDAR-derived DSM, which only records the maximum elevation value for a specific location without describing the vertical height heterogeneity. Future research could employ 3-D photo-realistic models, also available from the Hong Kong GeoData Store, to improve estimates of vertical shade distribution. The primary challenge for this issue is the design and construction of azimuth angle-based LUTs, which need to be expanded from 2-D maps (containing X and Y information) to 3-D data cubes (involving X, Y, and Z information).

5. Conclusion

The vital role of urban shade in shaping thermal environments and human behavior is often overlooked due to the lack of reliable and comprehensive shade datasets for entire cities. This study proposes a unique protocol to map citywide shade of Hong Kong using 3-D DSM data. The mapped shades achieve a high consistency with ground-based photo references and satellite imagery over both built and natural environments, with an agreement level ranging from 0.66 to 0.85. Solar geometry negatively correlates with the aggregation metrics of shade landscape and positively correlates with fragmented metrics, with the solar zenith angle exerting a stronger influence than the solar azimuth angle. Persistent shade from 3-D urban structure significantly reduces the sunlight hours, lowering the average daily sunlight time from 11 to 14 to 4–8 h. This study presents a cost-effective tool for quantifying citywide urban shade. The mapped datasets can be used for supporting sustainable urban design and planning that are related with 3-D urban

morphology, sunshine/shade resources, and energy system, such as cooling benefits of shade, and solar energy potential, and human access to sunlight.

CRediT authorship contribution statement

Shengbiao Wu: Writing – review & editing, Writing – original draft, Visualization, Formal analysis, Data curation. **Bin Chen:** Writing – review & editing, Writing – original draft, Supervision, Investigation, Funding acquisition, Formal analysis, Conceptualization. **Yimeng Song:** Writing – review & editing. **Jiafu An:** Writing – review & editing. **Chen Lin:** Writing – review & editing, Supervision, Funding acquisition. **Peng Gong:** Writing – review & editing, Supervision.

Declaration of competing interest

The authors declare that they have no known competing financial interests or personal relationships that could have appeared to influence the work reported in this paper.

Supplementary materials

Supplementary material associated with this article can be found, in the online version, at doi:10.1016/j.scs.2024.106011.

Data availability

Data will be made available on request.

References

Alhazmi, M., Sailor, D. J., & Anand, J. (2022). A new perspective for understanding actual anthropogenic heat emissions from buildings. *Energy and Buildings, 258*, Article 111860.

Armson, D., Stringer, P., & Ennos, A. (2012). The effect of tree shade and grass on surface and globe temperatures in an urban area. *Urban Forestry & Urban Greening, 11*(3), 245–255.

Bouillon, R. (2020). Vitamin D status in Africa is worse than in other continents. *The Lancet Global Health, 8*(1), e20–e21.

Biljecki, F., & Ito, K. (2021). Street view imagery in urban analytics and GIS: A review. *Landscape and Urban Planning, 215*, Article 104217.

Buo, I., Sagris, V., Jaagus, J., & Middel, A. (2023). High-resolution thermal exposure and shade maps for cool corridor planning. *Sustainable Cities and Society, 93*, Article 104499.

Calcabrini, A., Ziar, H., Isabella, O., & Zeman, M. (2019). A simplified skyline-based method for estimating the annual solar energy potential in urban environments. *Nature Energy, 4*(3), 206–215.

Cenci, L., Galli, M., Santella, C., Boccia, V., & Albinet, C. (2022). Analyzing the Impact of the Different Instances of the Copernicus DEM Dataset on the Orthorectification of VHR Optical Data. In *IGARSS 2022-2022 IEEE International Geoscience and Remote Sensing Symposium* (pp. 6001–6004). IEEE.

Chan, E. P. Y., Fung, T., & Wong, F. K. K. (2021). Estimating above-ground biomass of subtropical forest using airborne LiDAR in Hong Kong. *Scientific Reports, 11*(1), 1751.

Cheng, L., Zhang, F., Li, S., Mao, J., Xu, H., Ju, W., Liu, X., Wu, J., Min, K., & Zhang, X. (2020). Solar energy potential of urban buildings in 10 cities of China. *Energy, 196*, Article 117038.

Cherian, N. C., & Subasinghe, C. (2022). Sun-safe zones: Investigating integrated shading strategies for Children's play areas in urban parks. *International Journal of Environmental Research and Public Health, 20*(1), 114.

Cheung, P. K., & Jim, C. Y. (2019). Differential cooling effects of landscape parameters in humid-subtropical urban parks. *Landscape and Urban Planning, 192*, Article 103651.

Colter, K., Middel, A. C., & Martin, C. A. (2019). Effects of natural and artificial shade on human thermal comfort in residential neighborhood parks of Phoenix, Arizona, USA. *Urban Forestry & Urban Greening, 44*, Article 126429.

Compagnon, R. (2004). Solar and daylight availability in the urban fabric. *Energy and Buildings, 36*(4), 321–328.

De Abreu-Harbich, L. V., Labaki, L. C., & Matzarakis, A. (2015). Effect of tree planting design and tree species on human thermal comfort in the tropics. *Landscape and Urban Planning, 138*, 99–109.

Demuzere, M., Kittner, J., Martilli, A., Mills, G., Moede, C., Stewart, I. D., van Vliet, J., & Bechtel, B. (2022). A global map of local climate zones to support earth system modelling and urban-scale environmental science. *Earth System Science Data, 14*(8), 3835–3873.

Donovan, G. H.&, & Butry, D. T. (2009). The value of shade: Estimating the effect of urban trees on summertime electricity use. *Energy and Buildings, 41*(6), 662–668.

Dozier, J., & Frew, J. (1990). Rapid calculation of terrain parameters for radiation modeling from digital elevation data. *IEEE Transactions on Geoscience and Remote Sensing, 28*(5), 963–969.

Elgheznawy, D., & Eltarabily, S. (2021). The impact of sun sail-shading strategy on the thermal comfort in school courtyards. *Building and Environment, 202*, Article 108046.

Gage, R., Wilson, N., Signal, L., Barr, M., Mackay, C., Reeder, A., & Thomson, G. (2018). Using Google Earth to assess shade for sun protection in urban recreation spaces: Methods and results. *Journal of Community Health, 43*, 1061–1068.

Gilchrist, J. D., Morris, K. L., Dwyer, L. A., & Conroy, D. E. (2020). Patterns of sun safety behaviors in parents: Associations with physical activity, sedentary behavior, and access to neighborhood physical activity resources. *Preventive Medicine, 132*, Article 105976.

Gomez-Muñoz, V. M., Porta-Gándara, M., & Fernández, J. (2010). Effect of tree shades in urban planning in hot-arid climatic regions. *Landscape and Urban Planning, 94*(3–4), 149–157.

Gwedla, N., & Shackleton, C. M. (2019). Perceptions and preferences for urban trees across multiple socio-economic contexts in the Eastern Cape, South Africa. *Landscape and Urban Planning, 189*, 225–234.

Hesselbarth, M. H., Sciaini, M., With, K. A., Wiegand, K., & Nowosad, J. (2019). landscapemetrics: An open-source R tool to calculate landscape metrics. *Ecography, 42*(10), 1648–1657.

Holman, D. M., Kapelos, G. T., Shoemaker, M., & Watson, M. (2018). Shade as an environmental design tool for skin cancer prevention. *American Journal of Public Health, 108*(12), 1607–1612.

Horváthová, E., Badura, T., & Duchková, H. (2021). The value of the shading function of urban trees: A replacement cost approach. *Urban Forestry & Urban Greening, 62*, Article 127166.

Hua, J., Zhang, X., Ren, C., Shi, Y., & Lee, T.-C. (2021). Spatiotemporal assessment of extreme heat risk for high-density cities: A case study of Hong Kong from 2006 to 2016. *Sustainable Cities and Society, 64*, Article 102507.

Jay, O., Capon, A., Berry, P., Broderick, C., de Dear, R., Havenith, G., Honda, Y., Kovats, R. S., Ma, W., & Malik, A. (2021). Reducing the health effects of hot weather and heat extremes: From personal cooling strategies to green cities. *The Lancet, 398*(10301), 709–724.

Jiao, M., Zhou, W., Zheng, Z., Yan, J., & Wang, J. (2021). Optimizing the shade potential of trees by accounting for landscape context. *Sustainable Cities and Society, 70*, Article 102905.

Kaňuk, J., Gallay, M., & Hofierka, J. (2015). Generating time series of virtual 3-D city models using a retrospective approach. *Landscape and Urban Planning, 139*, 40–53.

Kong, F., Yan, W., Zheng, G., Yin, H., Cavan, G., Zhan, W., Zhang, N., & Cheng, L. (2016). Retrieval of three-dimensional tree canopy and shade using terrestrial laser scanning (TLS) data to analyze the cooling effect of vegetation. *Agricultural and Forest Meteorology, 217*, 22–34.

Kükenbrink, D., Schneider, F. D., Schmid, B., Gastellu-Etchegorry, J.-P., Schaepman, M. E., & Morsdorf, F. (2021). Modelling of three-dimensional, diurnal light extinction in two contrasting forests. *Agricultural and Forest Meteorology, 296*, Article 108230.

Lachapelle, J. A., Krayenhoff, E. S., Middel, A., Coseo, P., & Warland, J. (2023). Maximizing the pedestrian radiative cooling benefit per street tree. *Landscape and Urban Planning, 230*, Article 104608.

Lebègue, L., Cazala-Hourcade, E., Languille, F., Artigues, S., & Melet, O. (2020). CO3D, A worldwide one one-meter accuracy dem for 2025, *International Archives of the Photogrammetry. Remote Sensing & Spatial Information Sciences*.

Lee, L. S., Cheung, P. K., Fung, C. K., & Jim, C. Y. (2020). Improving street walkability: Biometeorological assessment of artificial-partial shade structures in summer sunny conditions. *International Journal of Biometeorology, 64*(4), 547–560.

Letu, H., Yang, K., Nakajima, T. Y., Ishimoto, H., Nagao, T. M., Riedi, J., Baran, A. J., Ma, R., Wang, T., & Shang, H. (2020). High-resolution retrieval of cloud microphysical properties and surface solar radiation using Himawari-8/AHI next-generation geostationary satellite. *Remote Sensing of Environment, 239*, Article 111583.

Li, D. H., Lau, C. C., & Lam, J. C. (2004). Overcast sky conditions and luminance distribution in Hong Kong. *Building and Environment, 39*(1), 101–108.

Li, X., & Ratti, C. (2018). Mapping the spatial distribution of shade provision of street trees in Boston using Google Street View panoramas. *Urban Forestry & Urban Greening, 31*, 109–119.

Li, X., Ratti, C., & Seiferling, I. (2018). Quantifying the shade provision of street trees in urban landscape: A case study in Boston, USA, using Google Street View. *Landscape and Urban Planning, 169*, 81–91.

Lindberg, F., & Grimmond, C. (2010). Continuous sky view factor maps from high resolution urban digital elevation models. *Climate Research, 42*(3), 177–183.

Lo, A. Y., & Jim, C. Y. (2015). Community attachment and resident attitude toward old masonry walls and associated trees in urban Hong Kong. *Cities, 42*, 130–141.

Luo, S., Li, H., & Shen, H. (2020). Deeply supervised convolutional neural network for shadow detection based on a novel aerial shadow imagery dataset. *ISPRS Journal of Photogrammetry and Remote Sensing, 167*, 443–457.

Mehta, V. (2008). Walkable streets: Pedestrian behavior, perceptions and attitudes. *Journal of Urbanism, 1*(3), 217–245.

Middel, A., AlKhaled, S., Schneider, F. A., Hagen, B., & Coseo, P. (2021). 50 grades of shade. *Bulletin of the American Meteorological Society, 102*(9), E1805–E1820.

Mogire, R. M., Mutua, A., Kimita, W., Kamau, A., Bejon, P., Pettifor, J. M., Adeyemo, A., Williams, T. N., & Atkinson, S. H. (2020). Prevalence of vitamin D deficiency in Africa: A systematic review and meta-analysis. *The Lancet Global Health, 8*(1), e134–e142.

Mountrakis, G., Im, J., & Ogole, C. (2011). Support vector machines in remote sensing: A review. *ISPRS Journal of Photogrammetry and Remote Sensing, 66*(3), 247–259.

Olsen, H., Kennedy, E., & Vanos, J. (2019). Shade provision in public playgrounds for thermal safety and sun protection: A case study across 100 play spaces in the United States. *Landscape and Urban Planning, 189*, 200–211.
Park, Y., Guldmann, J.-M., & Liu, D. (2021). Impacts of tree and building shades on the urban heat island: Combining remote sensing, 3D digital city and spatial regression approaches. *Computers, Environment and Urban Systems, 88*, Article 101655.
Rahman, M. A., Moser, A., Gold, A., Rötzer, T., & Pauleit, S. (2018). Vertical air temperature gradients under the shade of two contrasting urban tree species during different types of summer days. *Science of the Total Environment, 633*, 100–111.
Ratti, C., & Richens, P. (2004). Raster analysis of urban form. *Environment and planning B: Planning and Design, 31*(2), 297–309.
Schneider, S., Bolbos, A., Kadel, P., & Holzwarth, B. (2020). Exposed children, protected parents; shade in playgrounds as a previously unstudied intervention field of cancer prevention. *International Journal of Environmental Health Research, 30*(1), 26–37.
Shi, Y., Ren, C., Cai, M., Lau, K. K.-L., Lee, T.-C., & Wong, W.-K. (2019). Assessing spatial variability of extreme hot weather conditions in Hong Kong: A land use regression approach. *Environmental Research, 171*, 403–415.
Sivarajah, S., Thomas, S. C., & Smith, S. M. (2020). Evaluating the ultraviolet protection factors of urban broadleaf and conifer trees in public spaces. *Urban Forestry & Urban Greening, 51*, Article 126679.
Speak, A., Montagnani, L., Wellstein, C., & Zerbe, S. (2020). The influence of tree traits on urban ground surface shade cooling. *Landscape and Urban Planning, 197*, Article 103748.
Steger, C. R., Steger, B., & Schär, C. (2022). HORAYZON v1. 2: An efficient and flexible ray-tracing algorithm to compute horizon and sky view factor. *Geoscientific Model Development, 15*(17), 6817–6840.
Stoker, J., & Miller, B. (2022). The accuracy and consistency of 3d elevation program data: A systematic analysis. *Remote Sensing, 14*(4), 940.
Szokolay, S. V. (1996). *Solar geometry*. University of Queensland: Passive and Low Energy Architecture (PLEA) International in assoc. with Department of Architecture.
Taleghani, M., Swan, W., Johansson, E., & Ji, Y. (2021). Urban cooling: Which façade orientation has the most impact on a microclimate? *Sustainable Cities and Society, 64*, Article 102547.
Tan, P. Y., Wong, N. H., Tan, C. L., Jusuf, S. K., Chang, M. F., & Chiam, Z. Q. (2018). A method to partition the relative effects of evaporative cooling and shading on air temperature within vegetation canopy. *Journal of Urban Ecology, 4*(1), Juy012.
Troy, A., Taylor, R. V., Follingstad, G., & Heris, M. P. (2024). The impact of urban tree shade on residential irrigation demand in a semi-arid Western US City. *Sustainable Cities and Society, 100*, Article 105026.
Wang, C., Wang, Z.-H., Wang, C., & Myint, S. W. (2019). Environmental cooling provided by urban trees under extreme heat and cold waves in US cities. *Remote Sensing of Environment, 227*, 28–43.
Wong, N. H., Tan, C. L., Kolokotsa, D. D., & Takebayashi, H. (2021). Greenery as a mitigation and adaptation strategy to urban heat. *Nature Reviews Earth & Environment, 2*(3), 166–181.
Wu, S., Chen, B., An, J., Lin, C., & Gong, P. (2024). The interplay of cloud cover and 3D urban structures reduces human access to sunlight. *Nature Cities, 1*, 686–694.
Wu, S., Wen, J., You, D., Zhang, H., Xiao, Q., & Liu, Q. (2018). Algorithms for calculating topographic parameters and their uncertainties in downward surface solar radiation (DSSR) estimation. *IEEE Geoscience and Remote Sensing Letters, 15*(8), 1149–1153.
Wu, S., Yu, W., & Chen, B. (2023). Observed inequality in thermal comfort exposure and its multifaceted associations with greenspace in United States cities. *Landscape and Urban Planning, 233*, Article 104701.
Xu, Z., Etzel, R. A., Su, H., Huang, C., Guo, Y., & Tong, S. (2012). Impact of ambient temperature on children's health: A systematic review. *Environmental Research, 117*, 120–131.
Yu, Q., Ji, W., Pu, R., Landry, S., Acheampong, M., O'Neil-Dunne, J., Ren, Z., & Tanim, S. H. (2020). A preliminary exploration of the cooling effect of tree shade in urban landscapes. *International Journal of Applied Earth Observation and Geoinformation, 92*, Article 102161.
Zhang, Y., Chen, G., Vukomanovic, J., Singh, K. K., Liu, Y., Holden, S., & Meentemeyer, R. K. (2020). Recurrent Shadow Attention Model (RSAM) for shadow removal in high-resolution urban land-cover mapping. *Remote Sensing of Environment, 247*, Article 111945.
Zhu, R., Wong, M. S., You, L., Santi, P., Nichol, J., Ho, H. C., Lu, L., & Ratti, C. (2020). The effect of urban morphology on the solar capacity of three-dimensional cities. *Renewable Energy, 153*, 1111–1126.
Ziter, C. D., Pedersen, E. J., Kucharik, C. J., & Turner, M. G. (2019). Scale-dependent interactions between tree canopy cover and impervious surfaces reduce daytime urban heat during summer. *Proceedings of the National Academy of Sciences, 116*(15), 7575–7580.